Mutations in mouse *Aspm* (abnormal spindle-like microcephaly associated) cause not only microcephaly but also major defects in the germline

Jeremy N. Pulvers[a,1], Jarosław Bryk[b,2], Jennifer L. Fish[a,3], Michaela Wilsch-Bräuninger[a], Yoko Arai[a], Dora Schreier[a], Ronald Naumann[a], Jussi Helppi[a], Bianca Habermann[a,4], Johannes Vogt[c,5], Robert Nitsch[c,5], Attila Tóth[d], Wolfgang Enard[b], Svante Pääbo[b,6], and Wieland B. Huttner[a,6]

[a]Max Planck Institute of Molecular Cell Biology and Genetics, 01307 Dresden, Germany; [b]Max Planck Institute for Evolutionary Anthropology, 04103 Leipzig, Germany; [c]Institute for Cell Biology and Neurobiology, Center for Anatomy, Charité–Universitätsmedizin Berlin, 10115 Berlin, Germany; and [d]Institute of Physiological Chemistry, Technische Universität Dresden, 01307 Dresden, Germany

Contributed by Svante Pääbo, July 22, 2010 (sent for review June 25, 2010)

Mutations in *ASPM* (abnormal spindle-like microcephaly associated) cause primary microcephaly in humans, a disorder characterized by a major reduction in brain size in the apparent absence of nonneurological anomalies. The function of the Aspm protein in neural progenitor cell expansion, as well as its localization to the mitotic spindle and midbody, suggest that it regulates brain development by a cell division-related mechanism. Furthermore, evidence that positive selection affected *ASPM* during primate evolution has led to suggestions that such a function changed during primate evolution. Here, we report that in *Aspm* mutant mice, truncated Aspm proteins similar to those causing microcephaly in humans fail to localize to the midbody during M-phase and cause mild microcephaly. A human *ASPM* transgene rescues this phenotype but, interestingly, does not cause a gain of function. Strikingly, truncated Aspm proteins also cause a massive loss of germ cells, resulting in a severe reduction in testis and ovary size accompanied by reduced fertility. These germline effects, too, are fully rescued by the human *ASPM* transgene, indicating that ASPM is functionally similar in mice and humans. Our findings broaden the spectrum of phenotypic effects of *ASPM* mutations and raise the possibility that positive selection of *ASPM* during primate evolution reflects its function in the germline.

evolution | cerebral cortex | fertility | neural stem cells | germ cells

To understand the expansion of the cerebral cortex during mammalian evolution, it is necessary to identify the genes that determine cerebral cortical size during development (1). Genes that influence neural progenitor proliferation vs. differentiation are of particular interest, because the shifts in the balance between proliferation and differentiation may explain differences in brain size among mammals (2, 3). Genes in which mutations cause autosomal recessive primary microcephaly in humans, in which patients exhibit a major reduction in brain size in the apparent absence of nonneurological anomalies (4), can provide insight into mechanisms of progenitor cell division that operate in brain development (3).

ASPM (abnormal spindle-like microcephaly associated) (5) is an intriguing candidate gene for the regulation and evolution of brain size in the primate lineage (6) because *ASPM* mutations cause a substantial reduction in brain size, and the *ASPM* gene has been the target of positive selection during primate evolution (7–9). Of importance with regard to the underlying mechanism, the reduction in brain size in patients with *ASPM* mutations concerns all regions of the cerebrum and results in a reduced cortical surface area and a simplified gyral pattern (4, 10). This points to a defect in progenitor proliferation. Consistent with this, knockdown of *Aspm* in embryonic neural progenitors leads to an increase in asymmetric cell division and premature differentiation (3, 11), implicating the Aspm protein in the regulation of symmetric vs. asymmetric cell division, a crucial process in the balancing of progenitor proliferation vs. differentiation (3). In line with a role in cell division, Aspm localizes to mitotic spindle poles and the midbody (11–13).

ASPM mutations identified in microcephaly patients typically lead to protein truncation, with no correlation between the severity of the disorder and the length of the truncated protein (14, 15). This is consistent with the notion that the lack of the C-terminal domain of ASPM, which mediates midbody localization (13), may be sufficient to cause microcephaly in humans. However, although some nonneurological effects in microcephaly patients with *ASPM* mutations have been described (10, 16), it is unclear why other tissues are apparently much less affected than the brain although *Aspm* is expressed in many proliferating tissues (12, 17). Moreover, Aspm expression levels correlate with tumor progression (18, 19), and its knockdown leads to reduced proliferation of glioblastomas (20). In this context, mammalian Aspm may functionally differ from the *Drosophila* ortholog asp (abnormal spindle), which when mutated causes metaphase arrest in larval neuroblasts (21). In contrast, mouse neuroepithelial cells do not exhibit metaphase arrest upon knockdown (11).

To address these questions, we generated *Aspm* mutant mouse lines that mimic mutations found in human microcephaly patients. Furthermore, we introduced a human *ASPM* transgene into these mice to explore the function of human ASPM in the mouse.

Results and Discussion

Mutations in *Aspm* Cause Microcephaly in Mice. To study the function of Aspm in the development of the cerebral cortex and elsewhere, we generated two mutant mouse lines from gene trap ES cells (22), in which the endogenous protein is truncated and fused to a β-galactosidase and neomycin phosphotransferase fusion protein (β-geo). Basic characterization of these mouse lines with regard to *Aspm* mRNA expression and the Aspm–β-geo fusion proteins is described in *SI Results* (Fig. S1). The insertion site of the gene trap vector in ES cell line AJ0069 [Aspm$^{Gt(AJ0069)Wtsi}$]

Author contributions: J.N.P., A.T., W.E., S.P., and W.B.H. designed research; J.N.P., J.B., J.L.F., M.W.-B., Y.A., D.S., R. Naumann, B.H., and A.T. performed research; J.H., J.V., and R. Nitsch contributed new reagents/analytic tools; J.N.P. and W.B.H. analyzed data; and J.N.P., W.E., S.P., and W.B.H. wrote the paper.

The authors declare no conflict of interest.

[1]Present address: RIKEN Center for Developmental Biology, Kobe 650-0047, Japan.

[2]Present address: Max Planck Institute for Evolutionary Biology, 24306 Plön, Germany.

[3]Present address: Department of Craniofacial Development, King's College London, Guy's Hospital, SE19RT London, United Kingdom.

[4]Present address: Max Planck Institute for the Biology of Aging, 50931 Cologne, Germany.

[5]Present address: Institute for Microscopic Anatomy and Neurobiology, University Medicine Mainz, Johannes Gutenberg University Mainz, 55131 Mainz, Germany.

[6]To whom correspondence may be addressed. E-mail: paabo@eva.mpg.de or huttner@mpi-cbg.de.

This article contains supporting information online at www.pnas.org/lookup/suppl/doi:10.1073/pnas.1010494107/-/DCSupplemental.

was found to be between exons 25 and 26, and for AA0137 [Aspm$^{Gt(AA0137)Wtsi}$] between exons 7 and 8 (Fig. S1*A*). The mutant mice generated from AJ0069 and AA0137 will be referred to as *Aspm*$^{1-25}$ and *Aspm*$^{1-7}$ (1-25 and 1-7 in figures), respectively. The truncated *Aspm*$^{1-7}$ protein will contain only the microtubule-binding domain (Fig. S1*A*). In contrast, the predicted mutant protein in *Aspm*$^{1-25}$ mice only lacks the C-terminal amino acids encoded by the three 3′ exons but will retain the N-terminal microtubule-binding domain, the calponin homology domains, and the calmodulin-binding isoleucine-glutamine (IQ) repeats (12) (Fig. S1*A*). In this context, it is worth noting that all *ASPM* mutations identified in human microcephaly patients (with the exception of a missense mutation) truncate the protein in, or before, the region encoded by exon 26 (15, 23).

We first addressed whether mutations in Aspm cause microcephaly in mice. Because the clinical definition of human primary microcephaly is a reduction in brain size at birth, which does not progress in severity with age (4), we examined whether microcephaly is observed in newborn mice, on postnatal day (P) 0.5, and in adult mice (8–12 wk). In newborn mice, brains of *Aspm*$^{1-25}$- and *Aspm*$^{1-7}$-hom (homozygotes) were significantly reduced in weight compared with WT littermates (Fig. 1*A* and *D*), and interestingly, body weight was also reduced (Fig. 1*C*). Immunostaining for FoxP2, a deep-layer marker, and Brn1, an upper-layer marker, revealed normal cortical layering in *Aspm*$^{1-7}$-hom, in an apparently thinner cortex (Fig. 1*E*), indicating that the reduced brain weight was not due to defects in cortical layering or neuronal migration. Adult brains of homozygous *Aspm*$^{1-7}$ mutants showed a significant reduction in brain weight compared with WT (Fig. 1*G*), similar in proportion as in newborn mice (Fig. 1*D*); however, body weight was largely unchanged (Fig. 1*F*). As in humans, the effects of the mutant alleles were recessive because heterozygous (het) mice were indistinguishable from WT mice.

To analyze whether certain brain regions were affected more than others, we performed histological measurements on adult (8–9 wk) male brains. Serial coronal brain sections were Nissl stained, and a total of 15 sections, anatomically matched between brains, covering much of the rostrocaudal extent of the cerebral cortex, were analyzed (examples of rostral section in Fig. 1*H*, caudal section in Fig. 1*I*). Whole-section area (Fig. 1*J*) and the area of the six-layered neocortex (Fig. 1*K*, indicated in blue in Fig. 1 *H* and *I*) were measured. Data from WT and *Aspm*$^{1-7}$ heterozygotes (*Aspm*$^{1-7}$-het) were pooled and treated as control and were compared with littermate *Aspm*$^{1-7}$-hom. Results showed a significant reduction in whole-section (Fig. 1*J*) and neocortex (Fig. 1*K*) area in *Aspm*$^{1-7}$-hom compared with control. The mean area of the whole section and of the neocortex of *Aspm*$^{1-7}$-hom was reduced by a similar proportion (88.4% and 86.2% of control, respectively).

The same experiment was performed for *Aspm*$^{1-25}$-hom ($n = 10$) compared with littermate controls (WT and *Aspm*$^{1-25}$-het, $n = 8$). Whole-section area of the homozygote was 96.1% (not statistically significant) and of neocortex was 95.0% ($P < 0.05$) of control.

Thus, mutations in *Aspm* reduce brain size in mice, similar in nature to, albeit with less severity than, human primary microcephaly. Possible origins of this difference in severity, assuming that the *Aspm*$^{1-25}$ and *Aspm*$^{1-7}$ alleles are loss-of-function alleles equivalent to *ASPM* alleles causing microcephaly in humans, may lie in the difference in brain size itself. With a 1,000-fold larger cortical surface area, a longer neurogenic interval, and more progenitor divisions in humans compared with mice (1), potential effects caused by lack of Aspm function may accumulate and be more detrimental the more the progenitor cells divide. Alternatively, differences in the structure and/or the regulation of Aspm between humans and mice could be responsible for the different effects on brain size.

Human *ASPM* Transgene Rescues the Microcephaly Phenotype but Does Not Produce a Gain of Function in Mice. To be able to directly test the functional significance of the amino acid substitutions that

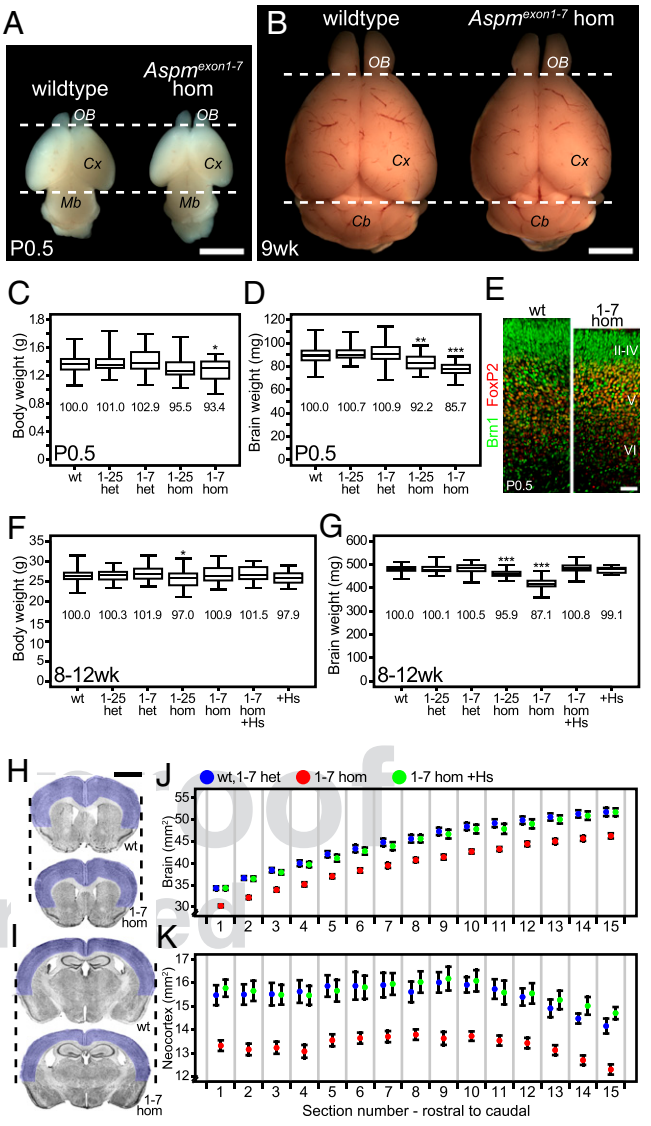

Fig. 1. Brain size analysis of *Aspm* mutant and human *ASPM* transgenic mice. (*A* and *B*) Brains from newborn (P0.5) and adult (9 wk) WT and *Aspm*$^{1-7}$-hom. Dashed lines delimit the rostrocaudal extent of the WT cerebral cortex (*Cx*). *OB*, olfactory bulb; *Mb*, midbrain; *Cb*, cerebellum. (Scale bar, 3 mm.) (*C* and *D*) Boxplot of whole body (*C*) and brain (*D*) weight of P0.5 WT and *Aspm*$^{1-25}$ (1-25) and *Aspm*$^{1-7}$ (1-7) heterozygous (het) and homozygous (hom) mice. Data from (left to right) 51, 34, 58, 18, and 22 mice. Mean weights compared with WT are indicated as percentages. (*E*) Double immunofluorescence for Brn1 (green) and FoxP2 (red) of vibratome sections (6-μm optical sections) of P0.5 neocortex. Cortical layers are indicated by II-VI. (Scale bar, 50 μm.) (*F* and *G*) Boxplot of whole-body (*F*) and brain (*G*) weight of adult (8–12 wk) WT, 1-25, and 1-7 het and hom, *Aspm*$^{1-7}$-hom with human *ASPM* BAC (1-7 hom +Hs), and WT mice with human *ASPM* BAC (+Hs). Data from (left to right) 65, 37, 27, 35, 59, 42, and 24 mice. Mean weights compared with WT are indicated as percentages. (*H* and *I*) Nissl staining of coronal 50-μm vibratome sections of adult brains from WT and 1-7 hom. Dashed lines delimit the lateral extent of the WT sections. Neocortex is highlighted in blue. Note the smaller size of the 1-7 hom brain. (Scale bar, 2 mm.) (*J* and *K*) Quantification of whole-brain (*J*) and neocortex (*K*) area across 15 sections along the rostrocaudal axis of control (WT and 1-7 het, $n = 9$, blue), 1-7 hom ($n = 20$, red), and 1-7 hom +Hs ($n = 12$, green). Sections in *H* and *I* are representative of sections 1 and 15 in the area quantifications, respectively. Data points indicate mean area (square millimeters); error bars indicate SEM. All data points of the 1-7 hom are significantly reduced ($P < 0.001$) compared with control. In boxplots (*C*, *D*, *F*, and *G*), the line within the box indicates the median value, the box spans the interquartile range, and whiskers extend to data extremes. *$P < 0.05$; **$P < 0.01$; ***$P < 0.001$.

have affected *ASPM* in the primate lineage (7–9) as well as to test unknown differences in Aspm regulation, we generated transgenic mice with a bacterial artificial chromosome (BAC) that contains the human *ASPM* locus. Qualitatively, embryos transgenic for human *ASPM* expressed *ASPM* mRNA (Fig. S1*B*) with the same spatial pattern as endogenous mouse *Aspm* (Fig. S2).

Mice transgenic for the human *ASPM* BAC exhibited normal brain (Fig. 1*G*) and body (Fig. 1*F*) weights, both in the WT background (+Hs in figures) and $Aspm^{1\text{-}7}$ homozygous background (1-7 hom +Hs in figures). Therefore, human *ASPM* can rescue the effects of mouse *Aspm* mutations. Results were further substantiated by the histological brain size measurements described above, which showed that the human *ASPM* BAC can fully rescue the microcephaly phenotype but does not produce a gain of function (Fig. 1 *J* and *K*). The full rescue, but lack of an increase in brain size beyond the WT level, has interesting implications as to the role of *ASPM* evolution with regard to brain development. In light of the evidence for positive selection of *ASPM*, our data do not exclude that the human protein may exert functions in the development of the human gyrencephalic brain that are not exerted by the mouse protein and to which the rodent model is not receptive. Be this as it may, our results imply that human ASPM can exert the function of mouse Aspm in the development of the rodent lissencephalic brain.

Midbody Localization Defects of Mutant Aspm Proteins. Immunofluorescence analysis of the subcellular localization of the $Aspm^{1\text{-}25}$ and $Aspm^{1\text{-}7}$ mutant proteins in mitotic neuroepithelial cells of embryonic day (E) 11.5 dorsal telencephalon showed that although the mutant proteins could localize to spindle poles in metaphase (Fig. S3*A*), they failed to localize to the midbody in telophase (Fig. S3*B*) (for details, see *SI Results*). These findings indicate that the N-terminal portion of Aspm encoded by the first seven exons is sufficient to direct metaphase spindle pole localization, whereas the lack of the C-terminal domain encoded by the last three exons is sufficient to cause a midbody localization defect (13). Furthermore, we found that the conserved C-terminal domain contains Armadillo repeats (Fig. S3*C*), which are lacking in the $Aspm^{1\text{-}7}$ mutant protein and disrupted in the $Aspm^{1\text{-}25}$ mutant protein, and disrupted in the most C-terminal mutation identified to date in microcephaly patients (10059C→A) (15, 23). Other proteins with Armadillo repeats have been shown to localize to the midbody and are crucial for cytokinesis (24). Because in the case of the $Aspm^{1\text{-}25}$ mutant, and in human patients, disruption of this domain alone causes microcephaly, this suggests that the Armadillo repeat may be crucial for proper Aspm function.

Analysis of Neural Progenitor Cell Function. Dysregulation of vertical cleavage planes of neuroepithelial and radial glial cells (collectively referred to as apical progenitors) to a more oblique and horizontal orientation, and hence their switch from symmetric to asymmetric division, can lead to premature differentiation and have consequences for brain size (3). However, quantitation of cleavage plane orientation of neuroepithelial cells of E11.5 dorsal telencephalon of $Aspm^{1\text{-}25}$ and $Aspm^{1\text{-}7}$ mutant mice revealed no major alterations compared with WT (Fig. S4 *A* and *B*). Likewise, no significant change in the ratio of symmetric vs. asymmetric cell divisions of $Aspm^{1\text{-}7}$-hom compared with WT was observed (Fig. S4 *C–E*) (for details, see *SI Results*).

Precocious differentiation of apical progenitors into neurons or downstream basal (intermediate) progenitors may lead to depletion of the apical progenitor pool and result in brain size reduction (2, 3). To address whether the microcephaly observed in *Aspm* mutants is due to premature differentiation, we quantified the proportion of *Tis21*-GFP+, neurogenic progenitors, and Tbr2+ basal progenitor cells in the embryonic dorsal telencephalon (Fig. S5 *A–C* and *D*, *Upper*). No significant change was observed in $Aspm^{1\text{-}7}$-hom compared with WT. The mitotic index of apical and basal progenitors also did not show a significant change (Fig. S5*D*, *Lower*) (for details, see *SI Results*).

In *Drosophila asp* mutants, neuroblasts become arrested in metaphase (21). By contrast, analysis of E11.5 dorsal telencephalon neuroepithelial cells of $Aspm^{1\text{-}25}$ and $Aspm^{1\text{-}7}$ mutant mice did not reveal a detectable metaphase block or defect in mitotic progression (Fig. S5 *E* and *F*) (for details, see *SI Results*).

In the cell counting at E11.5 and E13.5 described above (Figs. S4 and S5), no obvious increase in pyknotic nuclei, revealed by DAPI staining, was noticed in the two homozygotes compared with WT, indicating that an increase in apoptosis is not a likely explanation for the origin of the microcephaly.

The present results are in contrast to RNAi knockdown of Aspm, which led to increased asymmetric division (11). One possibility for this difference is that the present mutants generate truncated Aspm proteins that still localize to the mitotic spindle (Fig. S3*A*) and thus may partially fulfill the function of the full-length Aspm protein. Furthermore, alterations in mitotic cleavage plane orientation may only be achieved by acute ablation, such as by RNAi. In this context, it remains to be determined whether symmetric vs. asymmetric division is altered in human fetuses with *ASPM* mutations.

Mutations in *Aspm* Reduce Fertility in Males and Females. During the course of this study, we noticed that *Aspm* homozygous mutant mice exhibited a reduction in breeding efficiency. To systematically investigate the effects of *Aspm* mutations on fertility, mutant males and females were paired with C57BL/6 (BL6) females and males, respectively (Fig. 2). Plugs were observed in females of all genotypes at similar frequency, indicating that copulation frequency was not affected. $Aspm^{1\text{-}25}$ and $Aspm^{1\text{-}7}$ homozygous males mated with BL6 females exhibited a much lower pregnancy rate (number of pregnancies per plug) and also subtle changes in litter size (Fig. 2, *Left*). Interestingly, $Aspm^{1\text{-}25}$ and $Aspm^{1\text{-}7}$ heterozygous males exhibited an intermediate phenotype in pregnancy rate when mated with BL6 females. $Aspm^{1\text{-}25}$ and $Aspm^{1\text{-}7}$ homozygous females mated with BL6 males had significantly fewer embryos, and in the case of $Aspm^{1\text{-}7}$-hom females, also pregnancies (Fig. 2, *Right*). Taken together, results show that *Aspm* mutant males and females exhibit a reduction in pregnancy rate and offspring number.

Reduction in Sperm Count and Motility in *Aspm* Mutant Mice. Given the reduced fertility in *Aspm* homozygous males, we proceeded with an analysis of sperm. In live epididymal sperm observed by dark-field microscopy, we observed a much lower number of sperm in $Aspm^{1\text{-}7}$-hom compared with WT (Fig. 3*A*). To quantify epididymal sperm count, motility parameters, and morphometric features, freshly isolated epididymal sperm were analyzed in a sperm analyzer. The sperm count of $Aspm^{1\text{-}25}$- and $Aspm^{1\text{-}7}$-hom was ≈5- to 10-fold lower than in WT (Fig. 3*B*).

$Aspm^{1\text{-}25}$- and $Aspm^{1\text{-}7}$-hom showed a significant reduction in the proportion of total sperm that were motile or progressive (Fig. 3*C*). In addition, the following velocity parameters were measured: the track speed of motile sperm defined as the curvilinear velocity (VCL; Fig. 3*D*, dashed line), a smoothed average path velocity (VAP; Fig. 3*D*, dotted line), and the straight line velocity (VSL; Fig. 3*D*, solid line with arrowhead), which is calculated from the distance between the start and the end of the track. The two homozygotes showed a significant reduction in all three classes of sperm velocity parameters (Fig. 3*E*). Furthermore, sperm movement can be characterized by the ratios VSL/VCL, defined as linearity, which represents the linearity of the movement itself, and by VSL/VAP, defined as straightness, which represents the straightness of the track from beginning to end (Fig. 3*D*). No significant differences were observed in these two ratios (Fig. 3*E*), indicating that despite the reduction in velocity, the nature of movement did not differ. Interestingly,

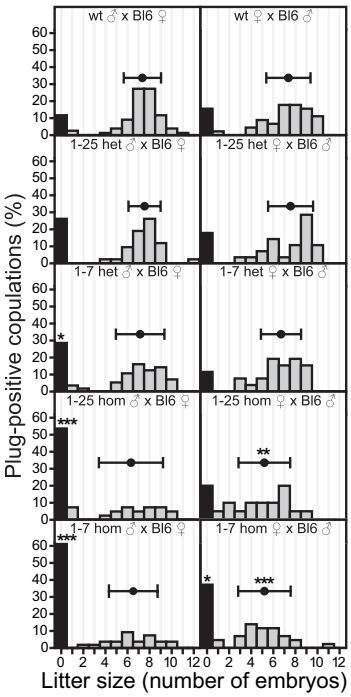

Fig. 2. Mutations in mouse *Aspm* reduce fertility in males and females. Frequency of occurrence of various litter sizes, expressed as percentage of all vaginal plug-positive copulations, for WT and 1-25 and 1-7 het and hom males (*Left*) and females (*Right*) paired with C57BL/6 females and males, respectively. Black columns indicate the percentage of females with no embryos (litter size = 0), gray columns the percentage of litters with embryos. Mean number of embryos in pregnant females is illustrated above the gray columns; horizontal error bars indicate SD. Data from (left, top to bottom) 74, 40, 55, 35, and 54 matings and (right, top to bottom) 45, 28, 26, 20, and 39 matings. $*P < 0.05$; $**P < 0.01$; $***P < 0.001$.

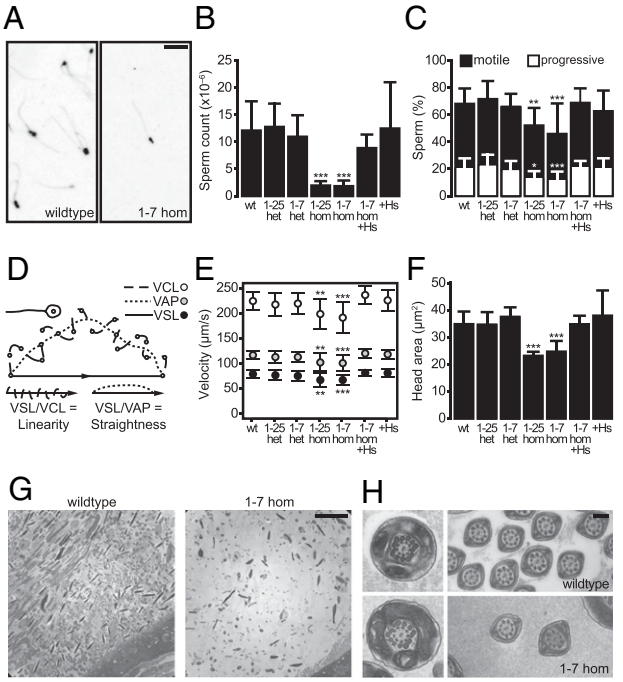

Fig. 3. Sperm analysis in *Aspm* mutant mice. (*A*) Dark-field image (inverted) of live epididymal sperm from WT and 1-7 hom mice. (Scale bar, 50 µm.) (*B*, *C*, *E*, and *F*) Epididymal sperm parameters of adult (8–12 wk) WT, 1-25 and 1-7 het and hom, 1-7 hom +Hs, and +Hs mice, obtained using the IVOS sperm analyzer. Data are the mean of (left to right) 21, 10, 11, 8, 13, 7, and 8 mice; error bars indicate SD; $*P < 0.05$; $**P < 0.01$; $***P < 0.001$. (*B*) Sperm count. (*C*) Percentage of sperm categorized as motile (black columns), of which a subset is categorized as progressive (white column segments). (*D*) Schematic illustration of sperm velocity parameters defined by the sperm analyzer: the track speed of motile sperm defined as the VCL (dashed lines), VAP (dotted lines), and VSL (solid line with arrowhead) calculated from the distance between the start and the end of the track. Furthermore, sperm movement can be characterized by the ratios VSL/VCL (linearity) and by VSL/VAP (straightness). (*E*) Sperm velocity parameters as defined in *D*: VCL (white circles), VAP (gray circles), and VSL (black circles). (*F*) Sperm head area. (*G* and *H*) Transmission electron microscopy of adult epididymis from adult WT (*G*, *Left*; *H*, *Upper*) and 1-7 hom (*G*, *Right*; *H*, *Lower*) mice. Note the reduction in cell density within the epididymis (*G*) and the normal axoneme ultrastructure (*H*) of the 1-7 hom compared with WT. (Scale bar, 10 µm in *G*; 200 nm in *H*.)

sperm from the two homozygotes showed a significant reduction in head area (Fig. 3*F*). However, the head shape, as defined by elongation (ratio of the minor to major axis of sperm head) did not differ, indicating that, despite the reduction in size, the sperm heads were morphologically normal. Importantly, all of the sperm parameter changes observed in $Aspm^{1-7}$-hom described above were rescued back to WT levels in $Aspm^{1-7}$-hom transgenic for the human *ASPM* BAC (Fig. 3 *B*, *C*, *E*, and *F*).

We next addressed, by transmission electron microscopy, whether the reduction in sperm motility and velocity was due to defects in the axoneme structure of the tail. Within the intact epididymis of $Aspm^{1-7}$-hom, the density of cells appeared drastically reduced compared with WT (Fig. 3*G*). Despite a reduction in sperm cells, the homozygote exhibited normal axoneme structure (Fig. 3*H*).

***Aspm* Mutations Cause Major Defects in the Male and Female Germlines.** We next investigated testes from newborn (P0.5), juvenile (P21), and adult (8–12 wk) homozygous mutant mice (Fig. 4*A*). At P0.5, testes from $Aspm^{1-7}$-hom appeared slightly reduced in size, and at P21 and in adults a dramatic reduction was observed. Testis weight was drastically reduced in $Aspm^{1-25}$- and $Aspm^{1-7}$-hom and rescued back to WT levels in $Aspm^{1-7}$-hom transgenic for the human *ASPM* BAC (Fig. 4*B*). In the seminiferous tubules of adult testes, Aspm was found to localize to the spindle poles of spermatogenic cells in metaphase (Fig. 4*C*) and at the midbody in telophase (Fig. 4*D*); these are subcellular localizations identical to those in neuroepithelial cells (Fig. S3 *A* and *B*).

A reduction in testicular size may be a reflection of the reduction in the number of germ cells within the seminiferous tubules (25). To investigate this, P0.5 testis sections were immunostained for the mouse vasa homolog (MVH; Fig. 4*E*), at this stage a marker of gonocytes or prespermatogonia (26). In WT P0.5 testes, essentially every tubule contained MVH+ cells (Fig. 4*E*, *Left*), whereas most tubules of $Aspm^{1-7}$-hom were lacking MVH+ cells (Fig. 4*E*, *Right*, and *F*). The number of MVH+ cells per tubule also showed a strong reduction (Fig. 4*G*). Thus, there was massive reduction of germ cells in $Aspm^{1-7}$-hom at birth.

Considering the reduction in adult testis size of the homozygotes, we investigated whether germ cells were still present in the seminiferous tubules of the adult testis by MVH immunostaining, at this stage a marker of spermatogenic cells from the spermatogonia to the round spermatid stage (26). In $Aspm^{1-7}$-hom, although spermatogenic cells were still present, many tubules did not contain MVH+ cells (Fig. 4*H*, *Right*). By DAPI staining (Fig. 4*I*), these empty tubules contained only Sertoli cells, which were identified by their characteristic centromeric heterochromatin condensed in two chromocenters (27) (Fig. 4*I*, *Inset*).

To investigate the origin of reduced fertility in *Aspm* homozygous mutant females, ovaries from adult (10–12 wk) mice were analyzed. Ovary weight was significantly reduced in $Aspm^{1-25}$- and $Aspm^{1-7}$-hom (Fig. 4*K*). We also analyzed whether there is a reduction in oocyte number, by immunostaining ovary sections

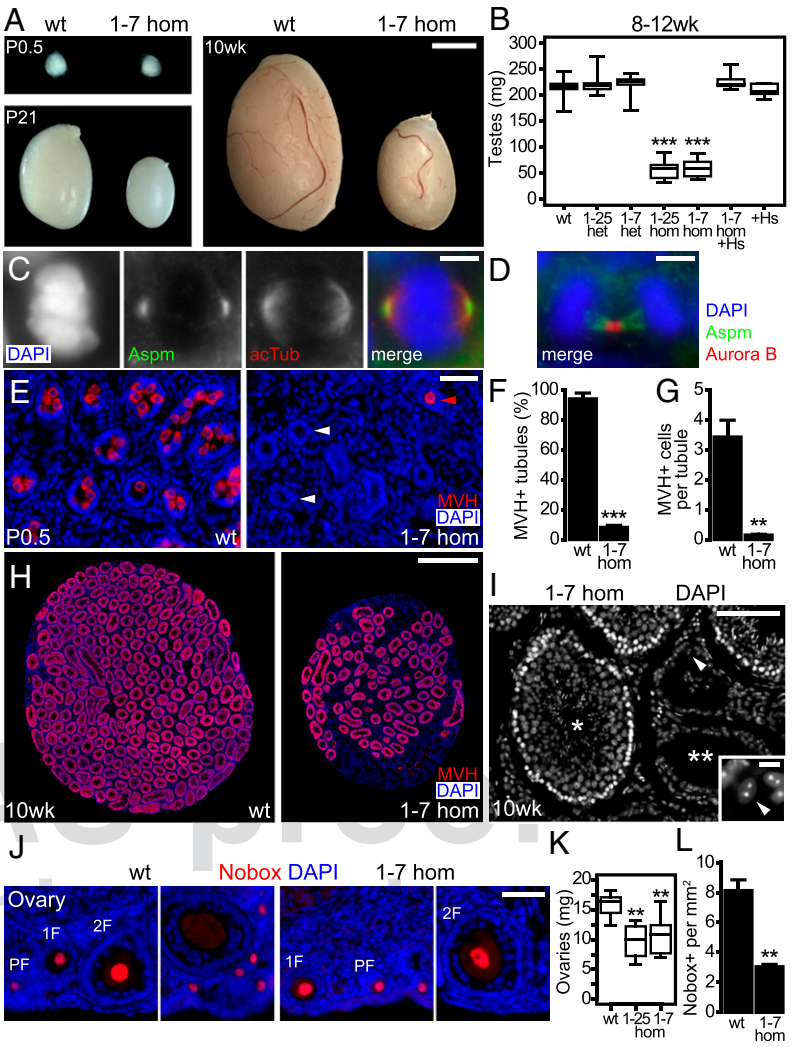

Fig. 4. *Aspm* mutations cause major defects in the male and female germlines. (*A*) Testes from newborn (P0.5), juvenile (P21), and adult (10 wk) WT and 1-7 hom mice. (Scale bar, 2 mm.) (*B*) Boxplot of testis weight (sum of left and right testis) of adult (8–12 wk) WT, 1-25 and 1-7 het and hom, 1-7 hom +Hs, and +Hs mice. Data from (left to right) 34, 13, 13, 12, 16, 7, and 10 mice. (*C* and *D*) Double immunofluorescence for Aspm (green) with acetylated α-tubulin (acTub, red) in *C*, and with Aurora B (red) in *D*, combined with DAPI staining (blue), of 10-μm cryosections (epifluorescence) of an adult testis from a WT mouse. A spermatogenic cell in metaphase is shown in *C*, and in telophase in *D*. (Scale bar, 5 μm.) (*E*) Immunofluorescence for MVH (red) with DAPI staining (blue) of 10-μm cryosections (epifluorescence) of testes from P0.5 WT (*Left*) and 1-7 hom (*Right*) mice. In WT, numerous MVH+ cells are found in the seminiferous tubules, whereas in 1-7 hom, most tubules lack germ cells (white arrowheads), and only a few tubules contain MVH+ gonocytes (red arrowhead). (Scale bar, 50 μm.) (*F* and *G*) Quantification of seminiferous tubules containing MVH+ cells, expressed as a percentage of the total number of tubules contained in testis sections (*F*), and the average number of MVH+ cells per seminiferous tubule in testis sections (*G*), from P0.5 WT and 1-7 hom mice. Data are the mean of testes from three mice (sum of five sections per testis). (*H*) Immunofluorescence for MVH (red) combined with DAPI staining (blue) of 10-μm cryosections (epifluorescence) of testes, cut orthogonally to the longitudinal axis, from 10-wk-old WT (*Left*) and 1-7 hom (*Right*) mice. In WT, essentially every seminiferous tubule contains MVH+ spermatogenic cells, whereas in 1-7 hom, only approximately half of the tubules contain MVH+ cells. (Scale bar, 1 mm.) (*I*) DAPI staining of a 10-μm cryosection (epifluoresence) of a testis from a 10-wk-old 1-7 hom mouse, showing a tubule containing spermatogenic cells (single asterisk), and empty tubules (double asterisk) containing only few Sertoli cells, identified by the characteristic centromeric heterochromatin condensed in two chromocenters revealed by DAPI staining (*Inset*). (Scale bar, 100 μm, 10 μm in *Inset*.) (*J*) Immunofluorescence for Nobox (red) combined with DAPI staining (blue) of 10-μm cryosections (epifluorescence) of ovaries from adult WT (*Left*) and 1-7 hom (*Right*) mice. All follicular stages—primordial (PF), primary (1F), secondary (2F), and antral follicles—were observed in WT and 1-7 hom ovaries. (Scale bar, 50 μm.) (*K*) Boxplot of ovary weight (sum of left and right ovary) of adult (10–12 wk) WT and 1-25 and 1-7 hom mice. Data from (left to right) 7, 4, and 9 mice. (*L*) Quantification of Nobox+ cells per total ovary section area from adult (10–12 wk) WT and 1-7 hom mice. Data are the mean of ovaries from three mice (sum of five sections per ovary). In boxplots (*B* and *K*), the line within the box indicates the median value, the box spans the interquartile range, and whiskers extend to data extremes. $^{**}P < 0.01$; $^{***}P < 0.001$.

for Nobox (Fig. 4*J*), a marker of oocytes in primordial, primary, secondary, and tertiary (antral) follicles (28). *Aspm*$^{1\text{-}7}$-hom ovaries appeared histologically normal, with follicles at the various stages readily identifiable (Fig. 4*J*). However, quantification of the number of Nobox+ oocytes (pooling all of the follicle stages) per ovary section area (including the corpus luteum) revealed an approximately 3-fold reduction in oocyte number in *Aspm*$^{1\text{-}7}$-hom compared with WT (Fig. 4*L*).

Because a large reduction in germ cells was observed already at birth in the male germline, that is, before the onset of germ cell differentiation and meiosis, this indicates that the origin of the defect is in either one, or a combination of (*i*) initial specification of primordial germ cells at E6.25–7.25, (*ii*) the subsequent proliferation of these cells, (*iii*) the migration of these cells to the genital ridge, and/or (*iv*) increased apoptosis during any of the above processes (29, 30). The additional germline defects observed, such as the reduction in sperm motility and head size, indicate further phenotypes seemingly unrelated to the initial loss of gonocytes.

Drosophila asp mutants also exhibit major germline defects, specifically in spermatogenesis and oocyte differentiation due to abnormal meiotic spindles, and also in germ cell proliferation (31, 32). Furthermore, studies in *Caenorhabditis elegans* show a role for Aspm in meiotic spindle organization (33). These phenotypes raise the possibility of pleiotropic effects of *Aspm* mutations in several aspects of the mammalian germline. *Aspm* mutant mice also showed a reduction in body weight at birth, which has been described for some human patients (10, 16), pointing to the possibility of additional defects in other organs.

Conclusion

The magnitude of the brain and germline phenotypes in the mice are in strong contrast, with the brain exhibiting only mild microcephaly, whereas the gonads exhibit a massive loss of germ cells. Primordial germ cells and undifferentiated primitive gonocytes are believed to be closely related to multipotent cells, because they express key markers of pluripotent cell lineages and give rise to teratomas and embryonic carcinomas in vivo and multipotent stem cells in vitro (34). Because the number of gonocytes was strongly reduced, *Aspm* mutations may be more detrimental to undifferentiated multipotent cells than to committed progenitor cells, such as those predominating in the developing brain during neurogenesis, which did not show any observable abnormality in the *Aspm* mutant mice. Accordingly, the mild microcephaly observed in the *Aspm* mutant mice may reflect a reduction in neural stem cells that took place already before the onset of neurogenesis; this would also explain the proportionality of the re-

duction in brain size. Furthermore, the finding that the proliferation of primordial germ cells seems to be affected upon *Aspm* mutation, together with the facts that *ASPM* is highly expressed in many cancers (12) and its expression levels correlate with tumor progression (18, 19), suggests a role for *ASPM* in the proliferative expansion of many different cell types.

The observation that *Aspm* mutations dramatically affect germline function raises a number of issues that should be addressed. The question arises whether germline defects similar to those seen in *Aspm* mutant mice are also present in patients with primary microcephaly caused by mutations in *ASPM*. Furthermore, our results raise the possibility that the positive selection of *ASPM* in the primate lineage may be related to the reproductive system rather than brain size (35). In fact, the detection of positive selection in *ASPM* relies on the observation of a high rate of nucleotide substitutions that affect the amino acid sequence of ASPM normalized to the rate of nucleotide substitutions that do not affect the protein. This effect is seen on the human evolutionary lineage, where it correlates with an increase in brain size, but also in chimpanzees and gorillas (8). Because evolutionary changes frequently affect spermatogenesis (36), these points taken together raise the possibility that selection on fertility, which is frequent among primates (37), may have influenced the evolution of *ASPM* in apes and humans.

Materials and Methods

Mouse Lines. Mouse lines were maintained in pathogen-free conditions in the animal facility of the Max Planck Institute of Molecular Cell Biology and Genetics (Dresden, Germany). Experiments were performed in accordance with German animal welfare legislation. Gene trap ES cells were obtained from the Sanger Institute Gene Trap Resource (Hinxton, Cambridge, United Kingdom). Details on mouse lines and genotyping are described in *SI Materials and Methods.*

Molecular, Morphological, and Functional Analyses. Tissue dissection, fixation, cryosectioning, vibratome sectioning, immunofluorescence, and Nissl staining were performed as previously described (*SI Materials and Methods*). Other methods of molecular, morphological, and functional analyses are described in *SI Materials and Methods.*

ACKNOWLEDGMENTS. We thank the Sanger Institute Gene Trap Resource (Hinxton, Cambridge, United Kingdom) for the gene trap ES cells; D. H. Douglas-Hamilton (Hamilton Thorne Inc.) and Drs. YoonJeung Chang and Jérôme Gilleron for discussions. J.N.P. and J.L.F. were members of the International Max Planck Research School for Molecular Cell Biology and Bioengineering. W.B.H. was supported by Deutsche Forschungsgemeinschaft Grant SFB 655, A2, the Deutsche Forschungsgemeinschaft-funded Center for Regenerative Therapies Dresden, and the Fonds der Chemischen Industrie.

1. Rakic P (2009) Evolution of the neocortex: A perspective from developmental biology. *Nat Rev Neurosci* 10:724–735.
2. Kriegstein A, Noctor S, Martínez-Cerdeño V (2006) Patterns of neural stem and progenitor cell division may underlie evolutionary cortical expansion. *Nat Rev Neurosci* 7:883–890.
3. Fish JL, Dehay C, Kennedy H, Huttner WB (2008) Making bigger brains—the evolution of neural-progenitor-cell division. *J Cell Sci* 121:2783–2793.
4. Woods CG (2004) Human microcephaly. *Curr Opin Neurobiol* 14:112–117.
5. Bond J, et al. (2002) ASPM is a major determinant of cerebral cortical size. *Nat Genet* 32:316–320.
6. Ponting C, Jackson AP (2005) Evolution of primary microcephaly genes and the enlargement of primate brains. *Curr Opin Genet Dev* 15:241–248.
7. Zhang J (2003) Evolution of the human ASPM gene, a major determinant of brain size. *Genetics* 165:2063–2070.
8. Kouprina N, et al. (2004) Accelerated evolution of the ASPM gene controlling brain size begins prior to human brain expansion. *PLoS Biol* 2:E126.
9. Mekel-Bobrov N, et al. (2005) Ongoing adaptive evolution of ASPM, a brain size determinant in *Homo sapiens*. *Science* 309:1720–1722.
10. Saadi A, et al. (2009) Compound heterozygous ASPM mutations associated with microcephaly and simplified cortical gyration in a consanguineous Algerian family. *Eur J Med Genet* 52:180–184.
11. Fish JL, Kosodo Y, Enard W, Pääbo S, Huttner WB (2006) Aspm specifically maintains symmetric proliferative divisions of neuroepithelial cells. *Proc Natl Acad Sci USA* 103: 10438–10443.
12. Kouprina N, et al. (2005) The microcephaly ASPM gene is expressed in proliferating tissues and encodes for a mitotic spindle protein. *Hum Mol Genet* 14:2155–2165.
13. Paramasivam M, Chang YJ, LoTurco JJ (2007) ASPM and citron kinase co-localize to the midbody ring during cytokinesis. *Cell Cycle* 6:1605–1612.
14. Bond J, et al. (2003) Protein-truncating mutations in ASPM cause variable reduction in brain size. *Am J Hum Genet* 73:1170–1177.
15. Nicholas AK, et al. (2009) The molecular landscape of ASPM mutations in primary microcephaly. *J Med Genet* 46:249–253.
16. Passemard S, et al. (2009) Expanding the clinical and neuroradiologic phenotype of primary microcephaly due to ASPM mutations. *Neurology* 73:962–969.
17. Lüers GH, Michels M, Schwaab U, Franz T (2002) Murine calmodulin binding protein 1 (Calmbp1): Tissue-specific expression during development and in adult tissues. *Mech Dev* 118:229–232.
18. Hagemann C, et al. (2008) Expression analysis of the autosomal recessive primary microcephaly genes MCPH1 (microcephalin) and MCPH5 (ASPM, abnormal spindle-like, microcephaly associated) in human malignant gliomas. *Oncol Rep* 20:301–308.
19. Lin S-Y, et al. (2008) ASPM is a novel marker for vascular invasion, early recurrence, and poor prognosis of hepatocellular carcinoma. *Clin Cancer Res* 14:4814–4820.
20. Horvath S, et al. (2006) Analysis of oncogenic signaling networks in glioblastoma identifies ASPM as a molecular target. *Proc Natl Acad Sci USA* 103:17402–17407.
21. do Carmo Avides M, Glover DM (1999) Abnormal spindle protein, Asp, and the integrity of mitotic centrosomal microtubule organizing centers. *Science* 283:1733–1735.
22. Skarnes WC, et al.; International Gene Trap Consortium (2004) A public gene trap resource for mouse functional genomics. *Nat Genet* 36:543–544.
23. Gul A, et al. (2007) Novel protein-truncating mutations in the ASPM gene in families with autosomal recessive primary microcephaly. *J Neurogenet* 21:153–163.
24. Wolf A, et al. (2006) The armadillo protein p0071 regulates Rho signalling during cytokinesis. *Nat Cell Biol* 8:1432–1440.
25. Chubb C (1992) Genes regulating testis size. *Biol Reprod* 47:29–36.
26. Toyooka Y, et al. (2000) Expression and intracellular localization of mouse Vasa-homologue protein during germ cell development. *Mech Dev* 93:139–149.
27. Hsu TC, Cooper JE, Mace ML, Jr, Brinkley BR (1971) Arrangement of centromeres in mouse cells. *Chromosoma* 34:73–87.
28. Suzumori N, Yan C, Matzuk MM, Rajkovic A (2002) Nobox is a homeobox-encoding gene preferentially expressed in primordial and growing oocytes. *Mech Dev* 111:137–141.
29. McLaren A (2003) Primordial germ cells in the mouse. *Dev Biol* 262:1–15.
30. Saitou M (2009) Germ cell specification in mice. *Curr Opin Genet Dev* 19:386–395.
31. Casal J, Gonzalez C, Wandosell F, Avila J, Ripoll P (1990) Abnormal meiotic spindles cause a cascade of defects during spermatogenesis in asp males of *Drosophila*. *Development* 108:251–260.
32. Riparbelli MG, Massarelli C, Robbins LG, Callaini G (2004) The abnormal spindle protein is required for germ cell mitosis and oocyte differentiation during *Drosophila* oogenesis. *Exp Cell Res* 298:96–106.
33. van der Voet M, et al. (2009) NuMA-related LIN-5, ASPM-1, calmodulin and dynein promote meiotic spindle rotation independently of cortical LIN-5/GPR/Galpha. *Nat Cell Biol* 11:269–277.
34. Kanatsu-Shinohara M, et al. (2004) Generation of pluripotent stem cells from neonatal mouse testis. *Cell* 119:1001–1012.
35. Ponting CP (2006) A novel domain suggests a ciliary function for ASPM, a brain size determining gene. *Bioinformatics* 22:1031–1035.
36. Findlay GD, Swanson WJ (2010) Proteomics enhances evolutionary and functional analysis of reproductive proteins. *Bioessays* 32:26–36.
37. Clark NL, Swanson WJ (2005) Pervasive adaptive evolution in primate seminal proteins. *PLoS Genet* 1:e35.

Supporting Information

Pulvers et al. 10.1073/pnas.1010494107

SI Results and Discussion

Generation of *Aspm* Mutant Mice. Two *Aspm* mutant mouse lines were generated from gene trap ES cells obtained from the Sanger Institute Gene Trap Resource. PCR and sequencing of genomic DNA revealed the insertion site of the gene trap vector to be between exons 25 and 26 for the ES cell line AJ0069, and between exons 7 and 8 for the AA0137 cell line (Fig. S1*A*). The mutant mice generated from AJ0069 and AA0137 will be referred to as $Aspm^{exon1\text{-}25}$ and $Aspm^{exon1\text{-}7}$ (1-25 and 1-7 in figures), respectively.

To demonstrate that the endogenous *Aspm* mRNA is lost in the two homozygous mutants, RT-PCR was performed on embryonic day (E) 13.5 whole-embryo RNA (Fig. S1*B*). In WT, only the endogenous WT transcript was present (Fig. S1*B*, *Left* and *Middle*, arrows), and in the heterozygotes, both WT and gene-trapped transcripts were present. However, in homozygotes, only the gene-trapped transcript was present (Fig. S1*B*, *Left* and *Middle*, arrowheads), providing evidence that the endogenous *Aspm* transcript was lost. To demonstrate that the Aspm protein is tagged with β-geo, we performed immunostaining for β-galactosidase (β-gal) together with Aspm, using an antibody against the exon 3–encoded sequence (1), on E10.5 dorsal telencephalon sections (Fig. S1*C*). In $Aspm^{exon1\text{-}7}$ heterozygotes and homozygotes, β-gal and Aspm colocalized at metaphase spindle poles (Fig. S1*C*, arrowheads), whereas β-gal immunoreactivity was lacking in the WT, providing evidence for the tagging of Aspm by β-geo. The same observation was made for $Aspm^{exon1\text{-}25}$ mice.

Generation of Human *ASPM* Transgenic Mice. Transgenic mice expressing the human *ASPM* gene were generated by using a bacterial artificial chromosome (BAC) that contains the human *ASPM* locus. RT-PCR on E13.5 whole-embryo RNA from WT and transgenic mice harboring the human BAC, using mouse *Aspm*-specific and human *ASPM*-specific primers, demonstrated the specific expression of the human transcript (Fig. S1*B*, *Right*). Furthermore, in situ hybridization using mouse *Aspm*-specific and human *ASPM*-specific probes showed that the BAC used directed human *ASPM* expression in the developing brain of transgenic mouse embryos with the same spatial pattern as endogenous mouse Aspm (Fig. S2).

Midbody Localization Defects Caused by Lack of Aspm C-Terminal Region. The subcellular localization of Aspm mutant proteins was investigated by using an antibody against the exon 3–encoded protein sequence (1) for immunostaining on E11.5 dorsal telencephalon sections, together with a centrosome marker, γ-tubulin (Fig. S3*A*), and a midbody marker, Aurora B (Fig. S3*B*). In WT, Aspm was found at spindle poles in metaphase and at the midbody in telophase (1–3). In $Aspm^{exon1\text{-}7}$ homozygotes, the mutant protein localized to metaphase spindle poles, although with weaker immunoreactivity compared with WT (Fig. S3*A*); however, no immunoreactivity was detected at the telophase midbody (Fig. S3*B*). The $Aspm^{exon1\text{-}25}$ mutant protein also localized to metaphase spindle poles (Fig. S3*A*), but the immunoreactivity at the telophase midbody was much reduced (Fig. S3*B*).

***Aspm* Mutant Mice Show No Detectable Effects in Orientation and Modes of Apical Progenitor Cell Division.** The cleavage plane orientation of apically dividing neuroepithelial cells of E11.5 dorsal telencephalon of *Aspm* mutant mice was quantified by measuring chromatid orientation, as revealed by DAPI staining, relative to the ventricular surface, as defined by phospho-vimentin (pVim) staining (Fig. S4*A*). Measurements were made on cells in metaphase (Fig. S4*B*, *Left*) and anaphase or telophase (Fig. S4*B*, *Right*). Results showed that the chromatid orientation of apically dividing cells were unchanged in the two homozygotes compared with WT, indicating that there are no major alterations in cleavage plane orientation in the present Aspm mutants.

To examine the regulation of symmetric vs. asymmetric cell division, in terms of the partitioning of cell constituents, in apically dividing neural progenitor cells, E11.5 dorsal telencephalon sections were immunostained for pan-cadherin to define, by lack of immunostaining, the apical plasma membrane (Fig. S4*C*), and to score in anaphase or telophase whether the predicted cleavage plane would bisect (symmetric) or bypass (asymmetric) the apical domain (1, 4). For this analysis, *Aspm* mutant mice were crossed with *Tis21*-GFP knock-in mice (5), to exclude from the analysis asymmetrically dividing cells (*Tis21*-GFP–positive) already committed to differentiative divisions (4). The actual cleavage plane angles measured in *Tis21*-GFP–negative anaphase or telophase cells of WT and $Aspm^{exon1\text{-}7}$ heterozygotes and homozygotes essentially all fell within 70° and 90° for symmetric divisions and were scattered between 60° and 90° for asymmetric divisions (Fig. S4*D*). Quantification of the proportion of symmetric and asymmetric divisions, expressed as a percentage of the total number of *Tis21*-GFP–negative anaphase or telophase cells analyzed (Fig. S4*E*), revealed no significant change in the ratio of symmetric vs. asymmetric cell divisions of the $Aspm^{exon1\text{-}7}$ homozygote compared with WT.

***Aspm* Mutant Mice Show No Detectable Effects on Neural Progenitor Proliferation and Differentiation During Neurogenesis.** To address whether the microcephaly observed in *Aspm* mutants is due to premature progression of neurogenesis, we quantified the proportion of *Tis21*-GFP–positive neurogenic cells, expressed as a percentage of total cells in the ventricular zone (VZ), delimited by TuJ1 immunostaining, in sections of E11.5 dorsal telencephalon (Fig. S5 *A* and *B*). No significant change was observed in the $Aspm^{exon1\text{-}7}$ homozygote compared with WT.

To address whether, in the mutants, there was a premature generation of basal progenitors (5–7), which would be at the expense of expanding neuroepithelial and radial glial cells, we performed Tbr2 immunostaining (8) and quantified the proportion of Tbr2-positive cells, expressed as a percentage of total cells in the cortical wall, in E13.5 dorsal telencephalon sections (Fig. S5 *C* and *D*, *Upper*). No significant change was observed in the $Aspm^{exon1\text{-}7}$ homozygote compared with WT. Sections were also immunostained for PH3 and TuJ1, to quantify the mitotic index of apical and basal progenitor cells in the VZ plus subventricular zone (SVZ; Fig. S5*D*, *Lower*). No significant change was observed in the $Aspm^{exon1\text{-}7}$ homozygote compared with WT.

To analyze whether neuroepithelial cells arrest in metaphase in *Aspm* mutant mice, E11.5 dorsal telencephalon sections were immunostained for PH3, which is positive from late G2 phase to anaphase (9), and pVim, which is positive throughout mitosis, from prophase to telophase (10), together with DAPI (examples in Fig. S4*A*). First, apical mitoses were categorized into either prometaphase and metaphase, or anaphase and telophase, as determined by DAPI staining, and the proportion out of all apical mitotic figures was calculated (Fig. S5*E*). Results showed that the percentage of the respective phases of mitosis were unchanged in the two homozygotes, indicating no alteration in the duration of these phases. Second, because pVim is positive throughout mitosis, but PH3 is only positive to anaphase, the pVim-positive but

PH3-negative staining reveals the proportion of cells in telophase (Fig. S5*F*). The proportion of PH3-positive and -negative cells expressed as a percentage of all pVim-positive cells was unchanged in the two homozygotes compared with WT. These results indicate that there is no detectable metaphase block or defect in mitotic progression of apically dividing neural progenitor cells in the present *Aspm* mutant mice.

SI Materials and Methods

Mouse Lines and Genotyping. *Aspm* gene trap mutant mouse lines were generated from ES cells [ID: AJ0069, $Aspm^{Gt(AJ0069)Wtsi}$; and AA0137, $Aspm^{Gt(AA0137)Wtsi}$; vector pGT0lxr; obtained from the Sanger Institute Gene Trap Resource] by blastocyst injection, and chimeras with germ line transmission were crossed to C57BL/6JOlaHsd. The exon immediately upstream of the vector insertion site, determined by 5′ RACE, was documented on the gene trap resource database (www.sanger.ac.uk/PostGenomics/genetrap). To determine the precise vector insertion site, PCR on ES cell genomic DNA was performed, using a forward primer targeting the upstream exon and a reverse primer targeting the 5′ end of β-geo, followed by sequencing. Primers used were the following: (exon7-F) 5′-GCCAAAAAGTCCTGAATTGG, (exon25-F) 5′-TTTGTTGTGATCCGAAGCTG, and (β-geo-R) 5′-AGTATCGGCCTCAGGAAGATCG. For the AJ0069 ES cell line, the insertion site was found to be in the intron between exon 25 and 26, 518 nt downstream from the intron start site, followed by vector sequence (starting at nt 288 downstream of the unique HindIII site); for the AA0137 ES cell line, the insertion site was found to be in the intron between exon 7 and 8, 1,386 nt downstream from the intron start site, followed by vector sequence (starting at nt 1,330 downstream of the HindIII site).

On the basis of the insert location, PCR primers for genotyping were designed. For AA0137 ($Aspm^{exon1\text{-}7}$) mice: (AA-F) 5′-GGGAAAGGCAAATGGAAAAC, (AA-Rgt) 5′-CCCAAGGCCATACAAGTGTT, and (AA-Rwt) 5′-ACCTCTCTGAGGAAGCACCA, with product size for WT allele 183 bp, gene trap allele 302 bp; for AJ0069 ($Aspm^{exon1\text{-}25}$) mice: (AJ-F) 5′-GAGACATAGCGGGTGAGAGC, (AJ-Rgt) 5′-CCTGGCCTCCAGACAAGTAG, and (AJ-Rwt) 5′-GCCTCACTAGCTGACACCACA, with product size for WT allele 161 bp, gene trap allele 307 bp.

Human *ASPM* transgenic mice were generated by pronuclear injection of a BAC that was linearized by NotI and purified on a Sepharose column. The BAC used (accession no. CTD-2353G2, vector pBELOBAC11) contains 136,600 bp of human genomic sequence, ≈41 kb of sequence 5′ to *ASPM* (downstream of the gene, because it is on the reverse strand), and 33 kb of sequence 3′ (upstream of the gene). Founder line screening and genotyping were performed by three primer pairs spanning the BAC: (L-F) 5′-ACACCCCACTGTCAATACTAGA, (L-R) 5′-GTCTTTGTCCTTACTGGGTTC, product size 404 bp; (M-F) 5′-CACCAGTGCTTGTAGGATAACT, (M-R) 5′-AGGAATCTAAGGTGTGCTAGTG, product size 601 bp; and (R-L) 5′-CACCTGAAGTTGGACCTTAAC, (R-R) 5′-TTGACCTACCTGACTGTAAACC, product size 767 bp.

Tis21-GFP knock-in mice were genotyped according to previously published protocols (5), and in experiments involving *Tis21*-GFP mice, a heterozygous background was used.

The day of the vaginal plug was defined as E0.5, and the day of birth was defined as postnatal day (P) 0.5.

RT-PCR. RT-PCR was performed using the OneStep RT-PCR Kit (Qiagen) on embryonic RNA extracted by the RNeasy Mini Kit (Qiagen). By using one forward primer targeting an exon upstream of the vector insertion site, and two reverse primers, one targeting the exon downstream of the insertion site and one targeting the 5′ end of β-geo, the endogenous transcript and the gene-trapped transcript could be distinguished. Primers for $Aspm^{exon1\text{-}7}$ mice: (exon6-F) 5′-CCGTACAGCTTGCTCCTTGT, (exon8-R) 5′-TCACTGTTGTCTGCCAGAGG, (5′_β-geo-R) 5′-GTTTTCCCAGTCACGACGTT with product size for WT transcript 231 bp, gene trap transcript 325 bp; for $Aspm^{exon1\text{-}25}$ mice: (exon25-F) 5′-TTTGTTGTGATCCGAAGCTG, (exon26-R) 5′-TCTCCAGGCTTCTCTCGGTA, (5′_β-geo-R) as above, with product size for WT transcript 179 bp, gene trap transcript 222 bp. Primers for mouse *Aspm*-specific RT-PCR: (Mm-F) 5′-AGCAGAAGCAGAATTCCTGTG, (Mm-R) 5′-TCCTTTTTGTCCCACACTGA, 211 bp; for human *ASPM*-specific RT-PCR: (Hs-F) 5′-GGTCCAAAGTTGTTGACCGTA, (Hs-R) 5′-CTTGCAGGGGATTTGTGATT; 219 bp.

Histology and Immunofluorescence Staining. Tissue dissection, fixation, cryosectioning, vibratome sectioning, immunofluorescence, and Nissl staining were performed as previously described (11). The following primary antibodies were used: Aspm (1), β-galactosidase (Z3781; Promega), Brn1 (sc-6028; Santa Cruz Biotechnology) (12), FoxP2 (ab16046; Abcam) (13), γ-tubulin (T6557; Sigma), Aurora B (611082; Becton Dickinson), phospho-histone H3 [06-570 (Millipore), ab10543 (Abcam)], phospho-vimentin (D076-3; MBL), pan-cadherin (C1821; Sigma), TuJ1 (mouse MMS-435P; rabbit MRB-435P; Covance), Tbr2 (ab23345; Abcam) (8), acetylated-α-tubulin (T6793; Sigma), MVH (ab13840; Abcam), and Nobox (ab41521; Abcam).

Quantification. Quantification of DAPI, PH3, pVim, *Tis21*-GFP, and Tbr2 staining was performed on 200-μm-wide fields of the dorsal telencephalon, with the ventricular surface being horizontal. For quantification of germ cells, P0.5 testes and adult ovaries were serially sectioned in a random orientation, and five sections spanning the organs were randomly chosen. MVH staining was used to identify gonocytes in testes, and Nobox staining to identify oocytes in ovaries.

Brain Size Measurements. Brains were dissected and weighed before fixation. For P0.5 mice, males and females were used, and for adult mice, to exclude heterogeneity caused by brain and body weight differences between male and female adult mice (www.jax.org/phenome), only males were used. For histological brain size measurements, brains were serially sectioned by a vibratome in the coronal orientation at 50-μm thickness. Nissl staining was performed on every fourth section in the region of interest (i.e., the cerebral cortex), such that a total of 15 sections were obtained for analysis. The area of the whole brain section and the area of the six-layered neocortex were measured using a Zeiss Axio Observer microscope and AxioVision software.

Electron Microscopy. Epididymides were dissected from 13-wk-old male mice and fixed in 1% glutaraldehyde and 2% paraformaldehyde in 0.1 M phosphate buffer at pH 7.4. The tissue was cut into small pieces, which were postfixed in 1% osmium tetroxide for 1 h at room temperature. Samples were dehydrated through a graded series of ethanol for standard embedding in EMBed-812 (Science Services). Ultrathin (70 nm) sections perpendicular to the epididymal tubules were cut on a Leica UCT ultramicrotome (Leica Microsystems), poststained with uranyl acetate and lead citrate, and viewed in a Morgagni electron microscope (FEI). Images were taken with a Veleta camera (Olympus).

In Situ Hybridization. In situ hybridization for mouse *Aspm* and human *ASPM* was performed using digoxigenin-labeled cRNA antisense probes, with human *ASPM* sense probe as a negative control, on cryosections by standard methods. Human *ASPM* probe corresponded to nucleotides 600–1,178 of the ORF, and mouse Aspm probe as previously described (1).

Protein Alignment and Domain Identification. The C-terminal region of human ASPM (amino acids 3,235–3,477) adjacent to the last isoleucine-glutamine (IQ) repeat was subjected to a PSI-BLAST search (14) using standard settings. The sequence picked up Armadillo repeats already at the second iteration. Multiple sequence alignments were done using ClustalW, and the alignment was manually refined and prepared for publication in Adobe Illustrator. Sequence accession nos. were as follows: *Homo sapiens* (NP_060606); *Pan troglodytes* (NP_001008994); *Macaca mulatta* (NP_001098005); *Equus caballus* (XP_001492636); *Bos taurus* (XP_614763); *Rattus norvegicus* (NP_001099425); and *Mus musculus* (NP_033921).

Fertility Testing. To analyze fertility, *Aspm* mutant males and females were paired with C57BL/6 females and males, respectively. Female mice in breeding cages were monitored daily for the presence of a vaginal plug, and when present were separated from the male. Pregnancy was assessed and embryo numbers were counted at postcoitum days 13.5 or 14.5 by dissection. The pregnancy rate was defined as the percentage of copulations resulting in pregnancy. WT mice, which were littermates to the mutant mice, were used as control. Some males were mated more than once. In some cases the mutant females were not dissected if nonpregnancy was obvious, were monitored that no pups were born, and then mated again to assess fertility. The mutant mice analyzed were between 8 and 25 wk of age, and the C57BL/6 mice used were between 8 and 15 wk of age, at the time of mating.

Sperm Analyses. To standardize the analysis of sperm, adult (8–12 wk old) virgin males were allowed to copulate once with a female as confirmed by vaginal plug, and were subjected to analysis 5 d later. To isolate sperm, intact epididymides were dissected, the surrounding fat tissue was carefully removed in 0.9% (wt/vol) NaCl, both epididymides were transferred to 170 μL cryoprotecting agent (CPA) solution [composed of 18% raffinose (R0250; Sigma) and 3% skim milk (0032-17-3; Difco)], ruptured with forceps, and incubated for 5 min at room temperature to release sperm. An aliquot (2 μL) of this sperm-containing suspension was transferred to 198 μL of HTF solution (15) and incubated for 5 min at 37 °C. An aliquot (25 μL) was taken and applied to Leja Standard Count 2 Chamber 100 Micron slides, and measurements were made on the IVOS Sperm Analyzer (Hamilton Thorne, version 12.3), with default settings for mouse sperm. In the case of the two homozygous mutants, measurements were also made, in parallel, with a 10-times-lower dilution factor (20 μL sperm-containing suspension into 180 μL HTF), to ensure similar levels of sperm sampling as WT for the acquisition of sperm velocity and morphology parameter data.

Statistics. Data processing, statistical analysis, and graph plotting were performed using the statistical programming language R (www.r-project.org). Student's *t* test was used for the calculation of all *P* values, with the exception of data with categorical variables: proportion of symmetric and asymmetric cell division (Fig. S4*E*), and the pregnancy rate data (Fig. 2 in main text), for which Fisher's exact test was used.

1. Fish JL, Kosodo Y, Enard W, Pääbo S, Huttner WB (2006) Aspm specifically maintains symmetric proliferative divisions of neuroepithelial cells. *Proc Natl Acad Sci USA* 103: 10438–10443.
2. Kouprina N, et al. (2005) The microcephaly ASPM gene is expressed in proliferating tissues and encodes for a mitotic spindle protein. *Hum Mol Genet* 14:2155–2165.
3. Paramasivam M, Chang YJ, LoTurco JJ (2007) ASPM and citron kinase co-localize to the midbody ring during cytokinesis. *Cell Cycle* 6:1605–1612.
4. Kosodo Y, et al. (2004) Asymmetric distribution of the apical plasma membrane during neurogenic divisions of mammalian neuroepithelial cells. *EMBO J* 23:2314–2324.
5. Haubensak W, Attardo A, Denk W, Huttner WB (2004) Neurons arise in the basal neuroepithelium of the early mammalian telencephalon: A major site of neurogenesis. *Proc Natl Acad Sci USA* 101:3196–3201.
6. Noctor SC, Martínez-Cerdeño V, Ivic L, Kriegstein AR (2004) Cortical neurons arise in symmetric and asymmetric division zones and migrate through specific phases. *Nat Neurosci* 7:136–144.
7. Miyata T, et al. (2004) Asymmetric production of surface-dividing and non-surface-dividing cortical progenitor cells. *Development* 131:3133–3145.
8. Englund C, et al. (2005) Pax6, Tbr2, and Tbr1 are expressed sequentially by radial glia, intermediate progenitor cells, and postmitotic neurons in developing neocortex. *J Neurosci* 25:247–251.
9. Hendzel MJ, et al. (1997) Mitosis-specific phosphorylation of histone H3 initiates primarily within pericentromeric heterochromatin during G2 and spreads in an ordered fashion coincident with mitotic chromosome condensation. *Chromosoma* 106:348–360.
10. Kamei Y, et al. (1998) Visualization of mitotic radial glial lineage cells in the developing rat brain by Cdc2 kinase-phosphorylated vimentin. *Glia* 23:191–199.
11. Pulvers JN, Huttner WB (2009) Brca1 is required for embryonic development of the mouse cerebral cortex to normal size by preventing apoptosis of early neural progenitors. *Development* 136:1859–1868.
12. McEvilly RJ, de Diaz MO, Schonemann MD, Hooshmand F, Rosenfeld MG (2002) Transcriptional regulation of cortical neuron migration by POU domain factors. *Science* 295:1528–1532.
13. Ferland RJ, Cherry TJ, Preware PO, Morrisey EE, Walsh CA (2003) Characterization of Foxp2 and Foxp1 mRNA and protein in the developing and mature brain. *J Comp Neurol* 460:266–279.
14. Altschul SF, et al. (1997) Gapped BLAST and PSI-BLAST: A new generation of protein database search programs. *Nucleic Acids Res* 25:3389–3402.
15. Quinn P, Kerin JF, Warnes GM (1985) Improved pregnancy rate in human in vitro fertilization with the use of a medium based on the composition of human tubal fluid. *Fertil Steril* 44:493–498.

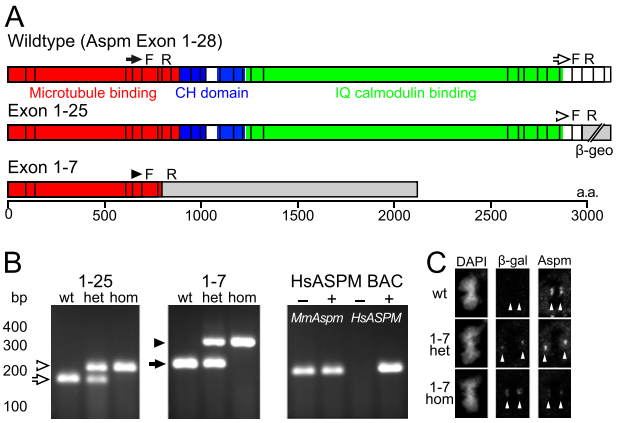

Fig. S1. *Aspm* mutant mice and *ASPM* humanized mice. (*A*) Scheme of mouse *Aspm* gene trap mutant proteins; WT, with 28 exons (*Top*), Aspm$^{exon1-25}$ (*Middle*), and Aspm$^{exon1-7}$ (*Bottom*). The major domains are indicated in colors, β-galactosidase/neomycin phosphotransferase (β-geo) in gray, and vertical lines separate exons. Arrows and arrowheads indicate primer pairs, the positions of which are indicated by letters (F, forward; R, reverse), and correspond to the RT-PCR products described in *B*. (*B*) RT-PCR on E13.5 whole-embryo RNA from *Aspm*$^{exon1-25}$ (*Left*), *Aspm*$^{exon1-7}$ (*Middle*), and human *ASPM* BAC transgenic (*Right*) mice. RT-PCR products are as follows: for *Aspm*$^{exon1-25}$, WT allele (179 bp) open arrow, gene-trapped allele (222 bp) open arrowhead; for *Aspm*$^{exon1-7}$, WT allele (231 bp) arrow, gene-trapped allele (325 bp) arrowhead; for human *ASPM* BAC transgenic (+) and littermate WT (–) mice, mouse *Aspm* (211 bp), human *ASPM* (219 bp). (*C*) Double immunofluorescence for β-gal and Aspm combined with DAPI staining of coronal cryosections (maximum intensity projection of three 1-μm optical sections) of E10.5 dorsal telencephalon. Note the colocalization of β-gal and Aspm immunoreactivity at the metaphase spindle poles (arrowheads) in the heterozygote and homozygote, demonstrating the tagging of the endogenous Aspm protein. Image width, 8.5 μm.

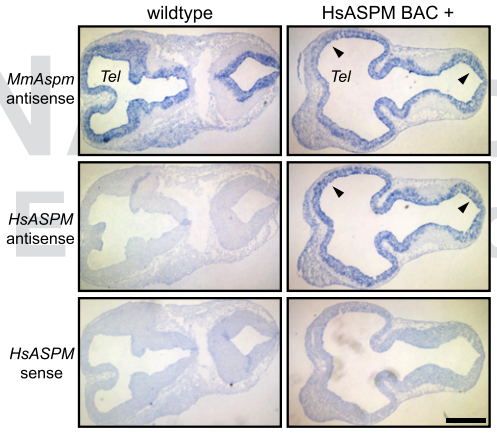

Fig. S2. *ASPM* BAC directs expression of human *ASPM* in transgenic mice with the same spatial pattern as endogenous mouse *Aspm*. In situ hybridization on transverse cryosections of E10.5 neural tube of WT (*Left*) and human *ASPM* BAC transgenic (HsASPM BAC +, *Right*) mice, from an independent founder line. Probes were as follows: mouse *Aspm*-specific antisense (*Top*), human *ASPM*-specific antisense (*Middle*), and human *ASPM*-specific sense (*Bottom*). Note the expression of human *ASPM* in the transgenic embryo, with the same spatial pattern as mouse *Aspm* (arrowheads). *Tel*, telencephalon. (Scale bar, 200 μm.)

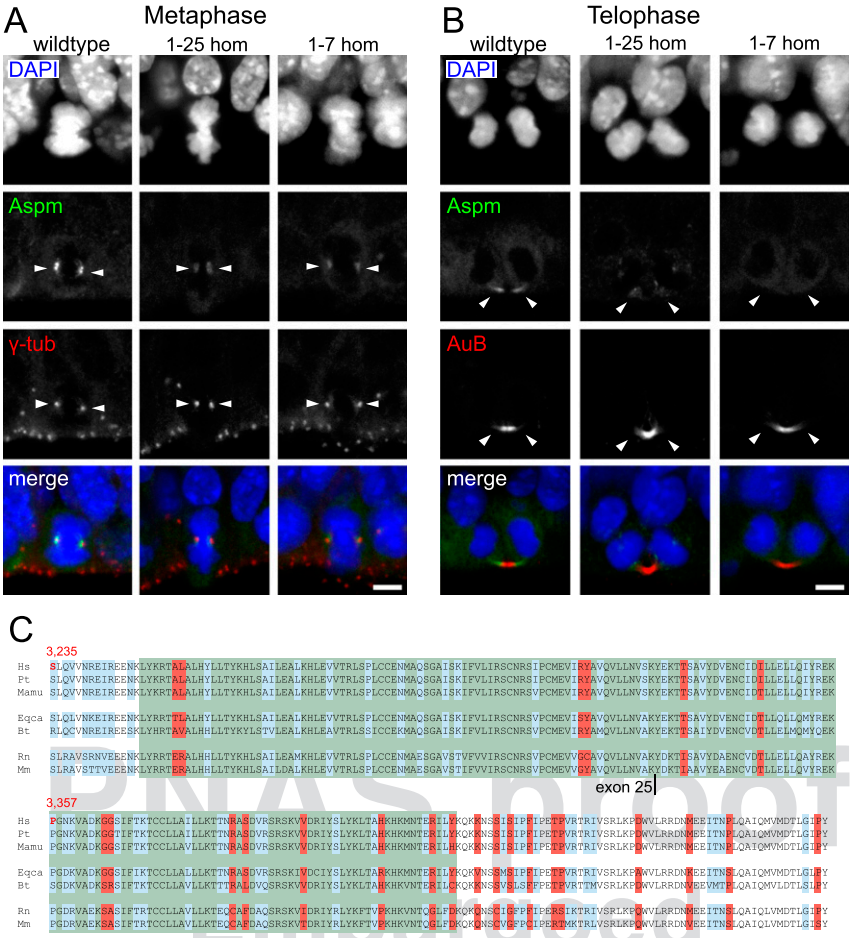

Fig. S3. Midbody localization defects caused by lack of Aspm C-terminal region. (*A* and *B*) Double immunofluorescence for Aspm (green) with γ-tubulin (γ-tub, red) in *A* and with Aurora B (AuB, red) in *B*, combined with DAPI staining (blue) of coronal cryosections (maximum intensity projection of two 1-μm optical sections) of E11.5 dorsal telencephalon of WT (*Left*) and *Aspm*$^{exon1-25}$ (*Middle*) and *Aspm*$^{exon1-7}$ (*Right*) homozygous mice. Cells in metaphase are shown in *A* and telophase in *B*. Note the Aspm immunoreactivity in the pericentrosomal region of cells in metaphase, indicated by arrowheads in *A*. Cells in telophase show Aspm immunoreactivity at the midbody, indicated by arrowheads in *B*, which is reduced in the *Aspm*$^{exon1-25}$ mutant and lacking in the *Aspm*$^{exon1-7}$ mutant. (Scale bar, 5 μm.) (*C*) Sequence alignment of mammalian Aspm proteins. Numbers refer to the amino acid residue in the human sequence (red letters). The region identifying Armadillo repeats is highlighted in green. Amino acids that differ between mammalian Aspm proteins are highlighted in blue and red. Blue indicates moderate and red indicates strong physico-chemical changes. Black line indicates the end of exon 25. Hs, human; Pt, chimpanzee; Mamu, macaque; Eqca, horse; Bt, cow; Rn, rat; Mm, mouse.

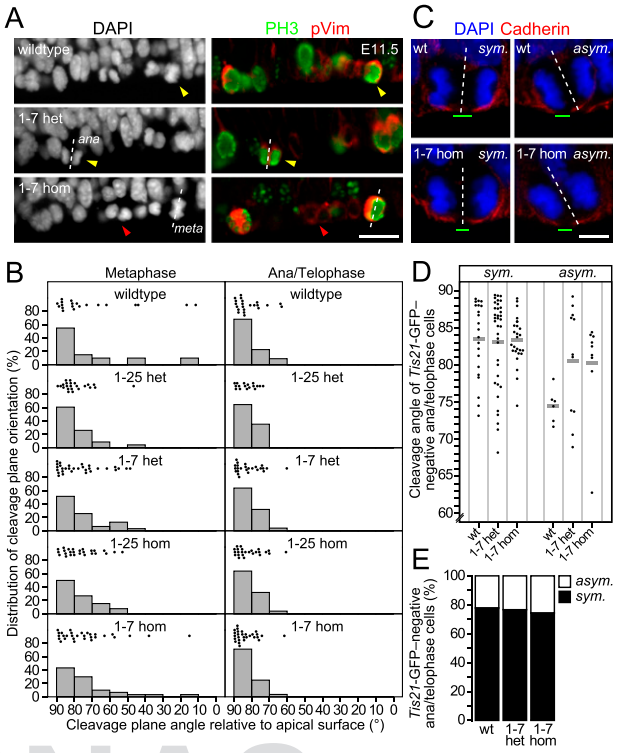

Fig. S4. Analysis of orientation and modes of neuroepithelial cell division in *Aspm* mutant mice. (*A*) Double immunofluorescence for phospho-histone H3 (PH3, green) and phospho-vimentin (pVim, red), combined with DAPI staining (white), of coronal cryosections (3-μm optical sections) of E11.5 dorsal telencephalon of WT and *Aspm*$^{exon1-7}$ heterozygous (het) and homozygous (hom) mice. Yellow arrowheads, double-positive cells; red arrowheads, pVim single-positive cell. Dashed lines indicate the predicted cleavage plane orientation quantified in *B*; meta, metaphase; ana, anaphase. (Scale bar, 20 μm.) (*B*) Histogram of the cleavage plane orientation, categorized into 10° bins (90°–81°, etc.) of apical mitotic cells in E11.5 dorsal telencephalon, as predicted by chromatid orientation in metaphase (*Left*) and anaphase or telophase (*Right*), defined by DAPI staining. Ninety degrees was defined as perpendicular to the ventricular surface. Single values (dots) are plotted above the histograms. For metaphase (from top), *n* = 20, 23, 31, 26, and 30 cells; ana/telophase (from top), *n* = 22, 17, 25, 25, and 28 cells; from four embryos per genotype. (*C*) Immunofluorescence for pan-cadherin (red) combined with DAPI staining (blue) of coronal cryosections (1-μm optical sections) of E11.5 dorsal telencephalon of WT and *Aspm*$^{exon1-7}$ homozygous (1-7 hom) mice in a *Tis21*-GFP heterozygous background (Fig. S5*A*). Dashed lines indicate the predicted cleavage plane; green bars indicate the cadherin hole. Symmetrically dividing (*sym.*, cadherin hole bisecting, *Left*) and asymmetrically dividing (*asym.*, cadherin hole bypassing, *Right*) cells are shown. (Scale bar, 5 μm.) (*D*) Quantification of the cleavage plane angle of symmetrically dividing (*sym.*) and asymmetrically dividing (*asym.*) *Tis21*-GFP–negative cells in anaphase or telophase determined as shown in *C*. Single data points (dots) are shown for WT, *Aspm*$^{exon1-7}$ (1-7) heterozygous (het) and homozygous (hom) mice. Horizontal bars indicate the mean. Data from: wt, 27; het; 47; hom; 35 cells, from three embryos per genotype. (*E*) Quantification of the proportion of symmetric (black columns) and asymmetric (white columns) cell divisions of *Tis21*-GFP–negative cells in anaphase or telophase, from WT, *Aspm*$^{exon1-7}$ (1-7) heterozygous (het) and homozygous (hom) mice. No significant changes were observed. Values were obtained from the data shown in *D*.

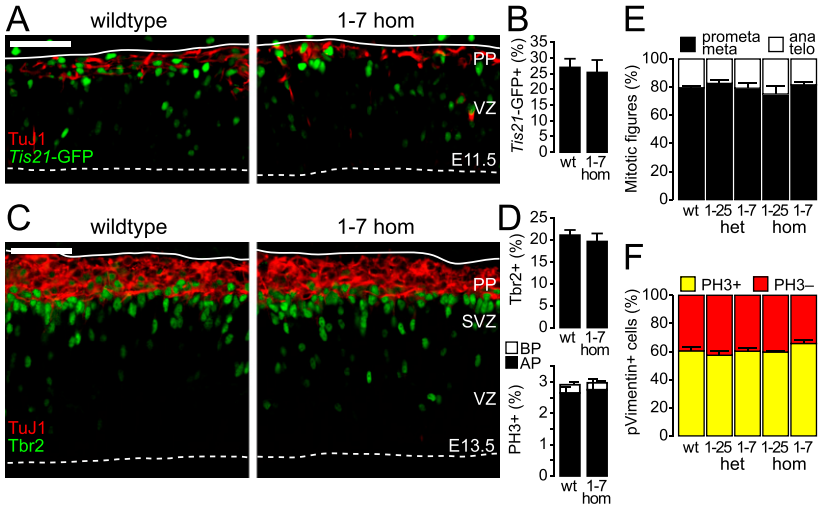

Fig. S5. Analysis of neural progenitor proliferation and differentiation in *Aspm* mutant mice. (*A*) Immunofluorescence staining for TuJ1 (red) with intrinsic *Tis21*-GFP fluorescence (green) of coronal cryosections (3-μm optical sections) of E11.5 dorsal telencephalon of WT (*Left*) and $Aspm^{exon1\text{-}7}$ homozygous (1-7 hom, *Right*) mice. VZ, ventricular zone; PP, preplate. (Scale bar, 50 μm.) (*B*) Quantification of *Tis21*-GFP–positive nuclei, expressed as a percentage of total nuclei as revealed by DAPI staining, in the VZ of E11.5 dorsal telencephalon of WT and $Aspm^{exon1\text{-}7}$ homozygous (1-7 hom) *Tis21*-GFP heterozygous mice. Data are the mean of three embryos (sum of three 200-μm-wide fields per embryo); error bars indicate SEM. (*C*) Double immunofluorescence staining for Tbr2 (green) and TuJ1 (red) of coronal cryosections (3-μm optical sections) of E13.5 dorsal telencephalon of WT (*Left*) and $Aspm^{exon1\text{-}7}$ homozygous (1-7 hom, *Right*) mice. SVZ, subventricular zone. (Scale bar, 50 μm.) (*D*) Quantification of Tbr2-positive nuclei, expressed as a percentage of total nuclei as revealed by DAPI staining, in the cortical wall of E13.5 dorsal telencephalon of WT and $Aspm^{exon1\text{-}7}$ homozygous (1-7 hom) mice (*Upper*), and quantification of PH3-positive apical (black column segments) and basal (white column segments) progenitor cells as a percentage of total nuclei in the VZ plus SVZ of E13.5 dorsal telencephalon of WT and $Aspm^{exon1\text{-}7}$ homozygous (1-7 hom) mice (*Lower*). Data are the mean of three embryos (sum of three 200-μm-wide fields per embryo); error bars indicate SEM. (*E*) Quantification of apical prometaphase plus metaphase cells (black column segments) and anaphase plus telophase cells (white column segments) expressed as a percentage of all apical mitotic cells, as determined by DAPI staining, in E11.5 dorsal telencephalon of WT and $Aspm^{exon1\text{-}25}$ (1-25) and $Aspm^{exon1\text{-}7}$ (1-7) heterozygous (het) and homozygous (hom) mice (Fig. S4*A*). Data are the mean of four embryos (sum of five 200-μm-wide fields per embryo); error bars indicate SEM. (*F*) Quantification of apical PH3 and pVim double-positive cells (yellow column segments) and apical pVim single-positive cells (red column segments), both expressed as a percentage of all apical pVim-positive cells, in E11.5 dorsal telencephalon of WT and $Aspm^{exon1\text{-}25}$ (1-25) and $Aspm^{exon1\text{-}7}$ (1-7) heterozygous (het) and homozygous (hom) mice (Fig. S4*A*). Data are the mean of four embryos (sum of five 200-μm-wide fields per embryo); error bars indicate SEM.